Welding in the World
https://doi.org/10.1007/s40194-025-01964-0

RESEARCH PAPER

Investigation of the microstructure and mechanical properties of dissimilar joints of PBF-LB/IN718 to AISI 316L by laser welding

Saeid Parchegani Chozaki[1] · Heidi Piili[1] · Shahriar Afkhami[2] · Mohsen Amraei[1] · Antti Salminen[1]

Received: 21 November 2024 / Accepted: 30 January 2025

Abstract

In this study, nickel-based superalloy, Alloy 718 (IN718), processed by powder bed fusion, was welded to wrought AISI 316L using laser welding. The effect of building direction, pre-weld heat treatment, and laser linear energy density on the weld strength of the dissimilar joints was examined. It was shown that employing a lower energy density improved the mechanical performance of the joints, resulting in the highest ultimate tensile strength. The joints in the as-built condition resulted in superior mechanical properties than the joints in heat treated condition. The hardness values of the joints were dependent on whether the PBF-LB/IN718 specimens were in heat-treated (HT) or as-built (AB) condition. The average hardness value at the fusion zone (FZ) of the HT joints was lower than that of the AB joints. Furthermore, the ductility of the HT joints was substantially reduced at higher energy densities while the AB joints showed relatively similar ductility at various energy densities. The loss of ductility was attributed to more pores formation at the FZ of the HT joints as a result of higher degree of oxide contamination following the heat treatment process. In this regard, these porosities can be deemed more detrimental to the joint than the solidification cracks (micro-cracks) following the secondary phases precipitations of Laves and carbides. Finally, the mechanical properties of the joints were unaffected by the build orientation of their additively manufactured base metal.

Keywords Additive manufacturing · Dissimilar laser welding · PBF-LB/IN718 · 316L · Microstructure · Mechanical properties

1 Introduction

Additive manufacturing (AM), also known as 3D printing, is an advanced technique for creating parts layer-by-layer directly from a CAD model. One of the most notable advantages of this technology over traditional manufacturing is the ability to produce highly complicated geometries due to more design flexibility from the layer-wise fabrication principle. Laser-based powder bed fusion (PBF-LB) has become more popular among additive manufacturing processes in various sectors, including aerospace, automotive, and medical due to its high resolution and near-net-shape fabrication [1, 2]. However, manufacturing large parts is one of the main challenges in AM due to the restriction in the size of the build platform and production chamber of AM machines, which hinders the broadening potential of PBF-LB for industrial applications [3]. Therefore, joining AM parts together using different welding technologies to produce larger assemblies could be a solution to address the part size limitation in the PBF-LB process. Laser welding has always been at the forefront of attention for industries as a highly efficient and fast process due to its high welding speed and precision [4]. Furthermore, laser welding offers benefits such as narrow heat-affected zones, low heat inputs, and minimized distortions which make laser welding an ideal choice for joining components with complex geometries [5].

Dissimilar welding of Alloy 718 and AISI 316L features a wide range of applications in aerospace, automotive, and nuclear power plants, wherever a combination of corrosive environment and high temperature is dominant as the service

---

Recommended for publication by Commission IV - Power Beam Processes

✉ Saeid Parchegani Chozaki
saeid.parcheganichozaki@utu.fi

[1] Department of Mechanical and Materials Engineering, University of Turku (UTU), Turku, Finland

[2] Laboratory of Steel Structure, LUT University, 53850 Lappeenranta, Finland

condition [6–10]. Welding of wrought Alloy 718 with AISI 316L or AISI 304 has been mostly carried out using the gas tungsten arc welding (GTAW) process as an inexpensive and easy to operate for onsite welding jobs [6–8]. However, some major drawbacks are associated with GTAW such as distortion, porosity, and lower welding speed due to high heat input that results in a wide and shallow weld zone [11]. Another concern regarding welding of Alloy 718 is its susceptibility to FZ cracking due to the segregation of niobium rich Laves phases which leads to lower joint strength and mechanical properties [12]. To address these issues, there have been some attempts to employ laser beam welding or electron beam welding (EBM) to join Alloy 718 with AISI 316L or AISI 304 since it provides lower heat input and higher welding speed. It has been shown that laser beam or EBM has significant impact on minimizing the Laves formation in the FZ compared to traditional GTAW due to its lower heat input and faster cooling rate [13]. Nevertheless, porosity formation during laser welding due to poor fluid ability of Alloy 718 compared to steel alloys is still a major problem that has been reported by some researchers [14]. The pore formation is particularity critical in laser beam welding due to faster cooling rate that prevents the trapped gasses in the FZ to escape from the keyhole [15].

There have been a few studies on the weldability of AM components, particularly when laser welding is used as a joining method. For example, Matilainen et al. [16] investigated the weldability of additively manufactured stainless steel and demonstrated that with optimized laser welding parameters (such as speed and power); it is possible to join PBF-LB/316L parts successfully. Yung et al. [17] examined the microstructure and mechanical behavior of laser-welded PBF-LB/304 stainless steel and showed that the fusion zone (FZ) has a coarser dendritic structure in comparison to the base metal, resulting in lower microhardness and tensile strength values. Another study by Wits et al. [18] showed that laser welding is a feasible technique to join PBF-LB/Ti-6Al-4 V parts together as well as to wrought Ti-6Al-4 V parts for aerospace application as no major defects, such as porosity or crack, was observed in the welded joint. Yu et al. [19] reported that performing heat treatment on the laser-welded specimens of PBF-LB/Ti-6Al-4 V results in lower microhardness, ultimate tensile strengths, yield strengths, and fatigue crack propagation rates in the fusion zones. Biffi et al. [20] conducted a study on the weldability of PBF-LB/AlSi$_{10}$Mg while laser welding is used and concluded that weldability of this alloy is acceptable; however, some challenges related to the high reflectivity and thermal conductivity still exist. These difficulties can result in pore formation in the fusion zone and deterioration of mechanical performance.

Further studies are required to better understand the mechanical and microstructural behavior of AM parts during and after laser welding due to the lack of published results in this area, especially for PBF-LB/IN718. Varparov et al. [21] demonstrated the possibility of utilizing laser welding for PBF-LB/IN718 with different thickness and reported that heat treatment has a noticeable effect on microstructure of welded samples in term of removing the residual stress. In another study, Jokish et al. [22] reported that laser welding of PBF-LB/IN718 pipes to PBF-LB/IN625 pipes could be effectively completed, although pores and cracks in the overlap area remained a significant problem to overcome due to the oscillation of keyhole during welding process.

In this study, laser welding is employed to join PBF-LB/IN718 to wrought AISI 316L, and the impact of the energy density on the quality of the welds is investigated by varying welding parameters such as power and welding speed. In addition, the effects of heat treatment, and the build orientation of the additively manufactured base metal on the microstructure, microhardness, and tensile performances of the joints are evaluated. To the knowledge of authors, the number of studies focused on the dissimilar welding of PBF-LB/IN718 to wrought alloys, e.g., wrought 316L to fabricate hybrid components (a combination of traditionally fabricated and additively manufactured parts) and structures, is currently very limited in the literature. Hence, this research indeed adds to our understanding of the feasibility of utilizing laser welding for AM parts and hybrid components, thus paving the way for the application of AM in large-scale manufacturing using the PBF-LB technique in conjunction with laser welding.

2 Materials and methods

2.1 Materials

For the additively manufactured base metal, the gas atomized Alloy 718 powder manufactured by EOS Finland Oy with an average particle size distribution of 20–50 µm was used for the PBF-LB process. AISI 316L stainless steel sheets were purchased from Outokumpu Oyj (Helsinki, Finland). The AISI 316L sheets were cut into 12 small samples with dimensions of 100 × 50 × 3 mm by using laser cutting with argon gas. The nominal chemical compositions of Alloy 718 powder and as-received AISI 316L are listed in Table 1.

2.2 Laser powder bed fusion of parts

The PBF-LB/IN718 samples were manufactured by Delva Oy (Hämeelinna, Finland) utilizing an EOS M290 machine. The machine is equipped with a single mode (SM) ytterbium fiber laser with a maximum power of 400 W and a building volume of 250 × 250 × 325 mm^3. The samples were fabricated using laser power of 285 W, scan speed 960 mm/s, layer thickness of 40 μm, and hatch distance of 0.11 mm with a rotation of 67° at each layer [23]. The building platform was preheated to 80 °C to reduce the thermal stress and prevent cracking between the parts and the build platform (stainless steel). The printing process was kept under a steady flow of argon gas to avoid oxidation. A total number of 12 samples were manufactured in two different vertical and horizontal build directions. The dimensions of experiment samples and building orientation are presented in Fig. 1.

2.3 Heat treatment of the BPF-LB/IN718 specimens

After manufacturing the PBF-LB//IN718 specimens, half of the samples were retained in the as-built condition (no stress relief or heat treatment was performed), while the rest were subjected to a solution annealing and aging heat treatment. The heat treatment was carried out to strengthen the additively manufactured base metal by precipitation of γ″ (Ni_3Nb) phase and releasing the residual stress accumulated during the AM process. The heat treatment procedure follows aerospace material specification standards of AM 2774 and AM 5662 and consists of three steps as listed in Table 2.

2.4 Laser welding

The experimental setup used for welding of the specimens is shown in Fig. 2. The setup consists of an IPG YLS-10000S fiber laser with a maximum average power of 10 kW and a central wavelength of 1070 nm. The laser beam was delivered by 200-μm optical fiber to the BIMO laser processing head (HIGHYAG™). The laser processing head included a collimation module with a focal length of 200 mm and a focusing module with a focal length of 250 mm, which generates a focal point diameter of 0.5 mm on the workpiece. A shielding gas nozzle (18 mm diameter) with a flow rate of about 20 L/min was attached to the laser processing head to protect the melt pool from the atmosphere by pumping argon to the welding zone. The shielding gas nozzle was angled 45° away from the component surface, following the welding direction from the backside. The joint edges were machined, and the oxide layer on the surface of the HT samples was removed manually using a rotary steel brush.

Laser welding parameters used in this study are listed in Table 3. These parameters were chosen after several trial and error on reaching a full penetration welding [24]. The linear energy density which is defined as the ratio of the laser input power to the welding speed is used as a main variable to

Table 1 Chemical composition of Alloy 718 powder and AISI 316L stainless steel (wt%)

Element	Fe	Ni	Cr	Mo	Nb	Ti	Al	C
Alloy 718	Bal	50.14	19.04	2.80	4.92	1.08	0.33	0.08
AISI 316L	Bal	10.00	17.20	2.02	-	-	-	0.02

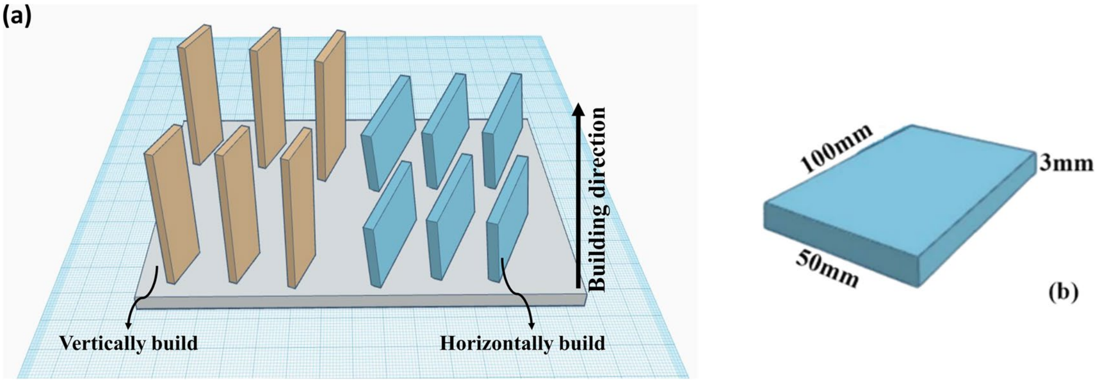

Fig. 1 **a** Schematic of PBF-LB/IN718 specimens with different build orientation, **b** dimension of PBF-LB/IN718 manufactured parts

Table 2 Heat treatment procedure

Heat treatment procedure	Temperature/time data
Solution annealing + aging	954 °C/1 h + air cooling + 718 °C/8 h + furnace cooling + 621 °C/18 h + air cool

study the impact of laser parameters on the microstructures and mechanical properties of the joints. Consequently, the linear energy density was increased from a lower value of 75 J/mm to a higher value of 120 J/mm as listed in Table 3.

The specimens were welded in two different types depending on the building orientation of PBF-LB/IN718 samples as illustrated in Fig. 3. The welding and building direction for the vertically printed samples are perpendicular (Fig. 3a), whereas the welding and building directions for the horizontally printed samples are parallel (Fig. 3b).

The joints are labeled as follows to make it easier to refer to each joint throughout the results and discussion section. Generally, the joints between heat-treated PBF-LB/IN718 and AISI 316L are abbreviated as HT joints, and the joints between as-built PBF-LB/IN718 and AISI 316L are abbreviated as AB joints. Furthermore, each joint is labeled depending on the build orientation, and laser welding parameters (Table 3) as presented in Table 4. For example, the joints between heat treated and horizontally manufactured PBF-LB/IN718 and AISI 316L are labeled as HTH, and depending on laser welding parameters used to join them, they are named HTH1, HTH2, and HTH3. In addition, for the purpose of simplicity, PBF-LB/IN718 and AISI 316L are referred to as AM 718 and 316L, respectively, on the images used in this paper.

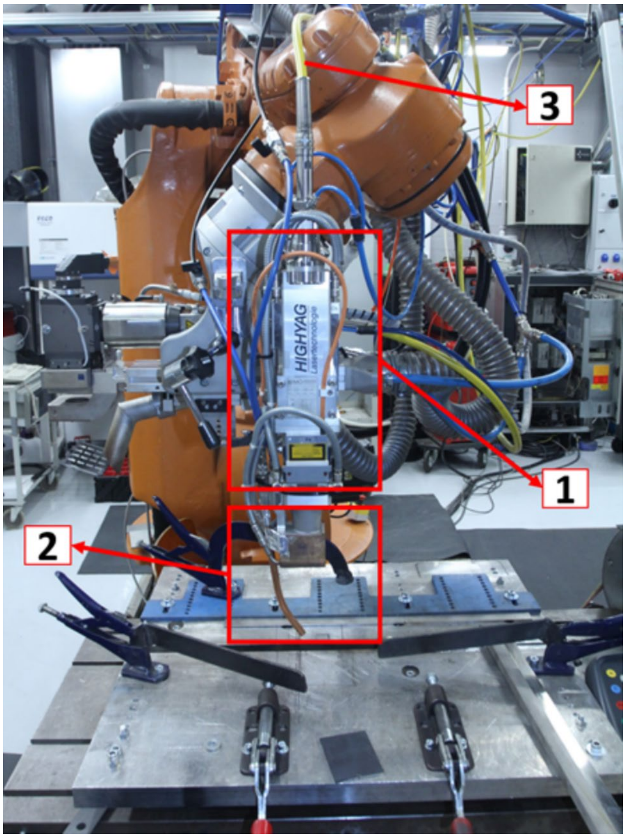

Fig. 2 Laser welding setup: (1) welding head, (2) shielding gas nozzle, (3) 200-µm optical fiber

Table 3 Laser welding parameters

Test number	Laser power (kW)	Welding speed (m/min)	Linear energy density (J/mm)	Focal point position (mm)	Gas flow rate (L/min)
#1	2.5	2.0	75	−2	20
#2	2.5	1.5	100	−2	20
#3	3.0	1.5	120	−2	20

2.5 Characterization of microstructure and mechanical properties

The metallographic samples were cut out of the cross-sections of the joints, and they were mounted in epoxy resin, fine ground, polished with diamond suspension, and electrolytically etched using Oxalic acid for 5 s. The microstructure characterizations were examined with a Wild M400 optical microscope and a Hitachi SU3500 scanning electron microscope (SEM). Energy dispersive spectroscopy (EDS) (operated at 10 kV) was used as a semi-quantitative technique to identify the chemical composition of the phases at the FZ. The uncertainty of the technique is discussed in the result section. An Empyrean X-ray diffractometer (with a Cu target) was used

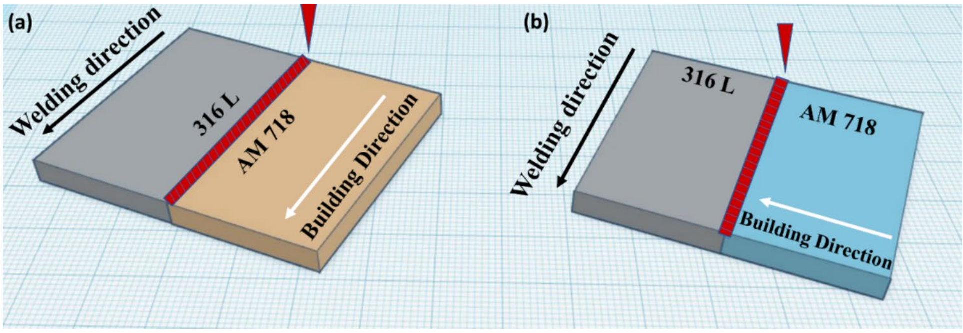

Fig. 3 Laser welding direction is **a** parallel to the building orientation of vertically printed PBF-LB/IN718, **b** perpendicular to the building orientation of horizontally printed PBF-LB/IN718

Table 4 Codenames used for the joints

Joint label	Description
HTH1; HTH2; HTH3	Heat treated and horizontally printed PBF-LB/IN718 to AISI 316L joint, welded by laser parameter set #1, #2, or #3, respectively
HTV1; HTV2; HTV3	Heat treated and vertically printed PBF-LB/IN718 to AISI 316L joint, welded by laser parameter #1, #2, and #3 respectively
ABH1; ABH2; ABH3	As-built and horizontally printed PBF-LB/IN718 to AISI 316L joint, welded by laser parameter #1, #2, and #3 respectively
ABV1; ABV2; ABV3	As-built and vertically printed PBF-LB/IN718 to AISI 316L joint, welded by laser parameter #1, #2, and #3 respectively

to identify the phases in the FZ and base metals. The beam size was narrowed down to approximately 1 mm using a 2-mm mask and a divergence slit of 1/16° at the incident beam side. Rietveld analysis was employed to refine the X-ray patterns using X-pert high score software. The experimental data was analyzed using standard X-ray patterns that were extracted from Inorganic Crystal Structure database (ICSD). Struers DuraScan 70 was utilized to measure the Vickers microhardness per EN ISO 6507. The applied load and holding time were 3 kgf and 15 s, respectively. The tensile tests were carried out using a servo-hydraulic system with a rated force capacity of 50 kN at room temperature and a displacement rate of 0.025 mm/s. Three tensile samples were tested for each joint, and the average results of ultimate tensile, 0.2% offset yield strength, and elongation were reported. The tensile samples were cut using laser cutting and then machined to the following dimensions per ASTM E-8, as shown in Fig. 4. The surface roughness of the HT samples was measured before and after the oxide removal process on five different samples using Alicona InfinitFocus optical surface measurement device using a minimum horizontal resolution of 3 µm and vertical resolution of 2 nm. The measurement area was 5×5 mm^2, and the average results were reported according to ISO 12781–1–2003 standard.

3 Results and discussion

3.1 Weld bead geometry

The cross-sectional micrographs of some the HT joints and AB joints are presented in Fig. 5. Generally, full penetration welding is observed in all the joints using all three laser welding parameters. Furthermore, all the joints are crack-free at the FZ, showing that laser welding is a feasible technique to join these dissimilar materials and could be used for AM material. However, the HT joints show higher porosity than the AB joints. This issue is especially notable at higher energy densities of 120 J/mm, in which the HTV3 joint shows an incomplete filled groove (Fig. 5f); nevertheless, it is still categorized as weld quality level B according to ISO 13919–1 and is permitted for welding applications.

The average weld cross section area of the HT joints observed to be 10% less than the AB joints. This could be resulted from the oxide removal process in which the surface roughness Ra and Rz of the HT sample were reduced roughly by 11.1% and 9.2% respectively as reported in Table 5. The relationship between surface roughness and absorptivity rate in laser welding is discussed in other studies [16] which aligns with the finding of this work.

Further, it is noted that the HT joints exhibit higher degree of spatters than the AB joints as seen in Fig. 6. Spatter formation is a complex phenomenon that generates as a result of molten metal ejection from the keyhole due to vapor

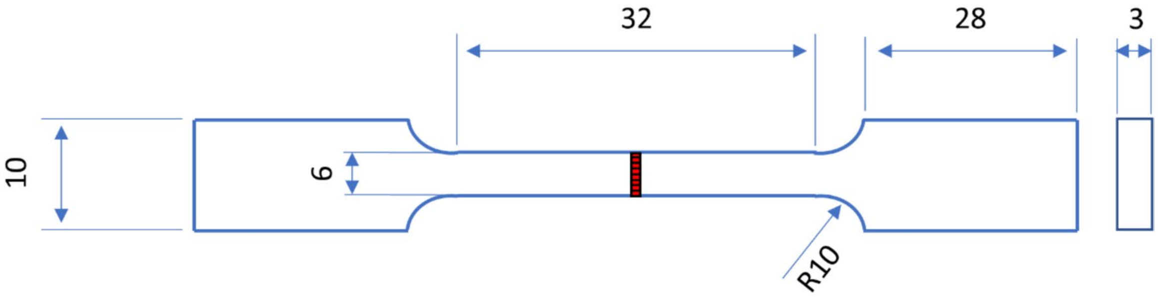

Fig. 4 Dimension of the tensile samples (dimensions in mm)

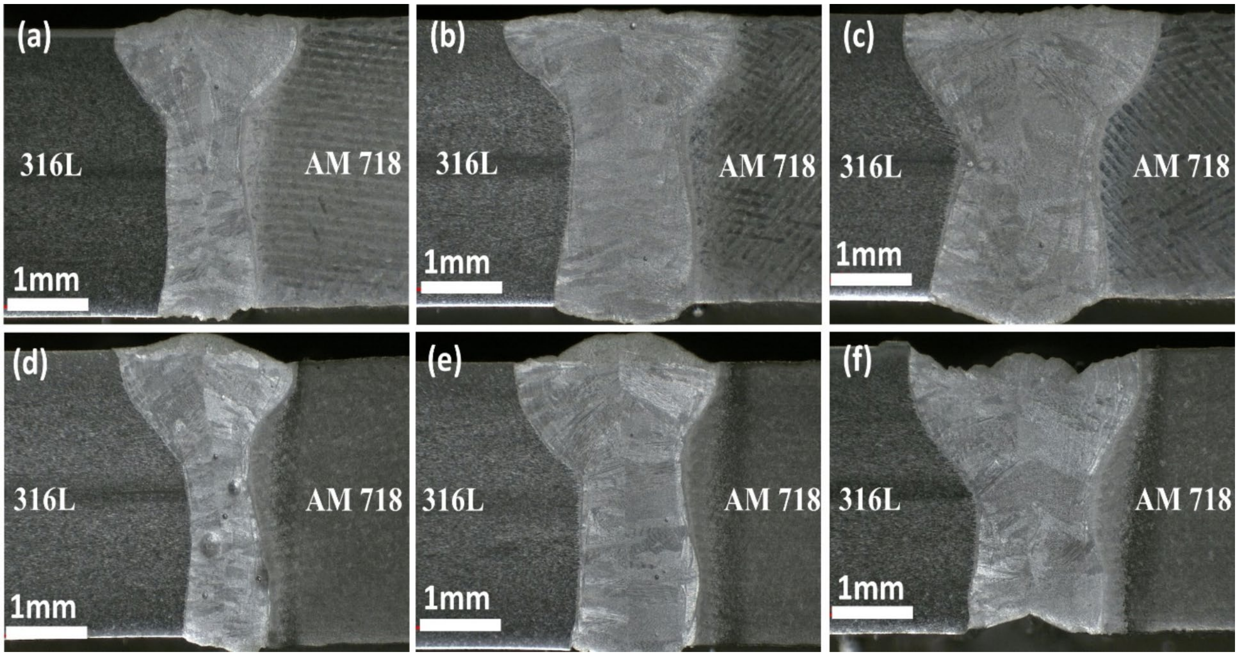

Fig. 5 Cross-section micrographs of HTV and ABV joints. **a** ABV1, **b** ABV2, **c** ABV3, **d** HTV1, **e** HTV2, **f** HTV3

Table 5 Surface roughness measurement of the HT samples before and after oxide removal process

Surface roughness	Ra (µm)	Rz (µm)
As-manufactured	5.3 ± 0.2	41 ± 1.5
After oxide removal	4.7 ± 0.2	37 ± 2.0

pressures gradient on the keyhole walls or fluctuation of the keyhole itself which accelerate the fluid flow surrounding the keyhole [25, 26]. Moreover, spatter is influenced by the welded materials characteristics and laser welding parameters. Regarding the laser welding parameters, studies have reported that increasing the energy input as a result of higher welding power could lead to greater degree of spatter formation which is in line with the observation of this study [14]. Regarding the welded material characteristic, surface tension, viscosity, and thermal conductivity are considered to be significant material characteristics that could have a direct impact on the formation of spatter [25]. Surface contaminations are one of the important factors that could directly impact the surface tension thus influencing the spatter formation [26]. In this regard, the higher degree of spatters in the HT samples could be correlated to the higher surface contamination (oxide layer) of the HT samples following the heat treatment process. The heat treatment process in this study was performed in a furnace without argon gas thus resulted in oxide layer formation on the HT samples. Although, the oxide layer was removed before welding, it seems that the removal process was unsuccessful in completely removing the oxide layer. According to some studies [27], the oxide layer growth in IN718 is proportional to

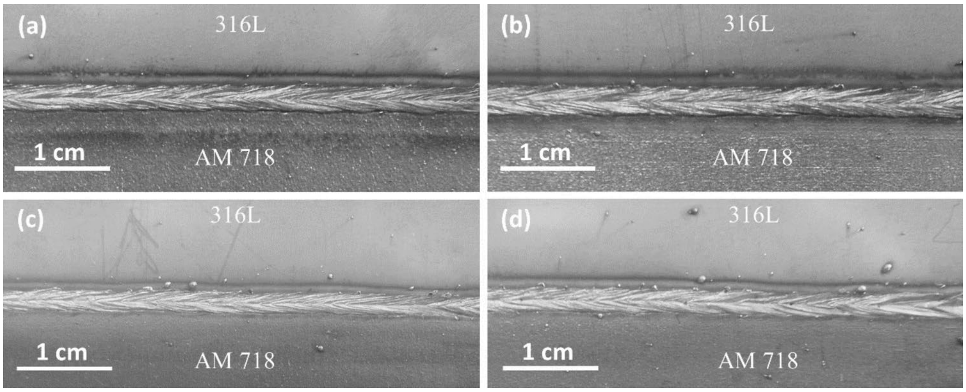

Fig. 6 Top surface of the joints, welded at linear energy density of 120 J/mm. **a** ABH3, **b** ABV3, **c** HTH3, **d** HTV3

the heat treatment temperature and could build up to 40 µm thickness at temperature as high as 1000 °C. Therefore, the residual of oxide layer in this study could be the source of contamination on the HT sample during welding, leading to increased spatter formation. However, it should be mentioned that using a sandpaper with a lower grit could be better option for removing oxide layer; however, it could alter the thickness of the material. For this reason, a rotary brush was employed in this work to minimize the impact of the oxide removal process on the thickness of the samples.

3.2 Microstructure characteristics

3.2.1 As-built PBF-LB/IN718

The microstructures of the as-built PBF-LB/IN718, which are built horizontally (Fig. 7a) and vertically (Fig. 7b), are shown in Fig. 7. The growth direction of the grains in the horizontally made samples is elongated in the building direction and exhibits a columnar morphology, as shown in Fig. 7a. According to the figure, the grains' orientation

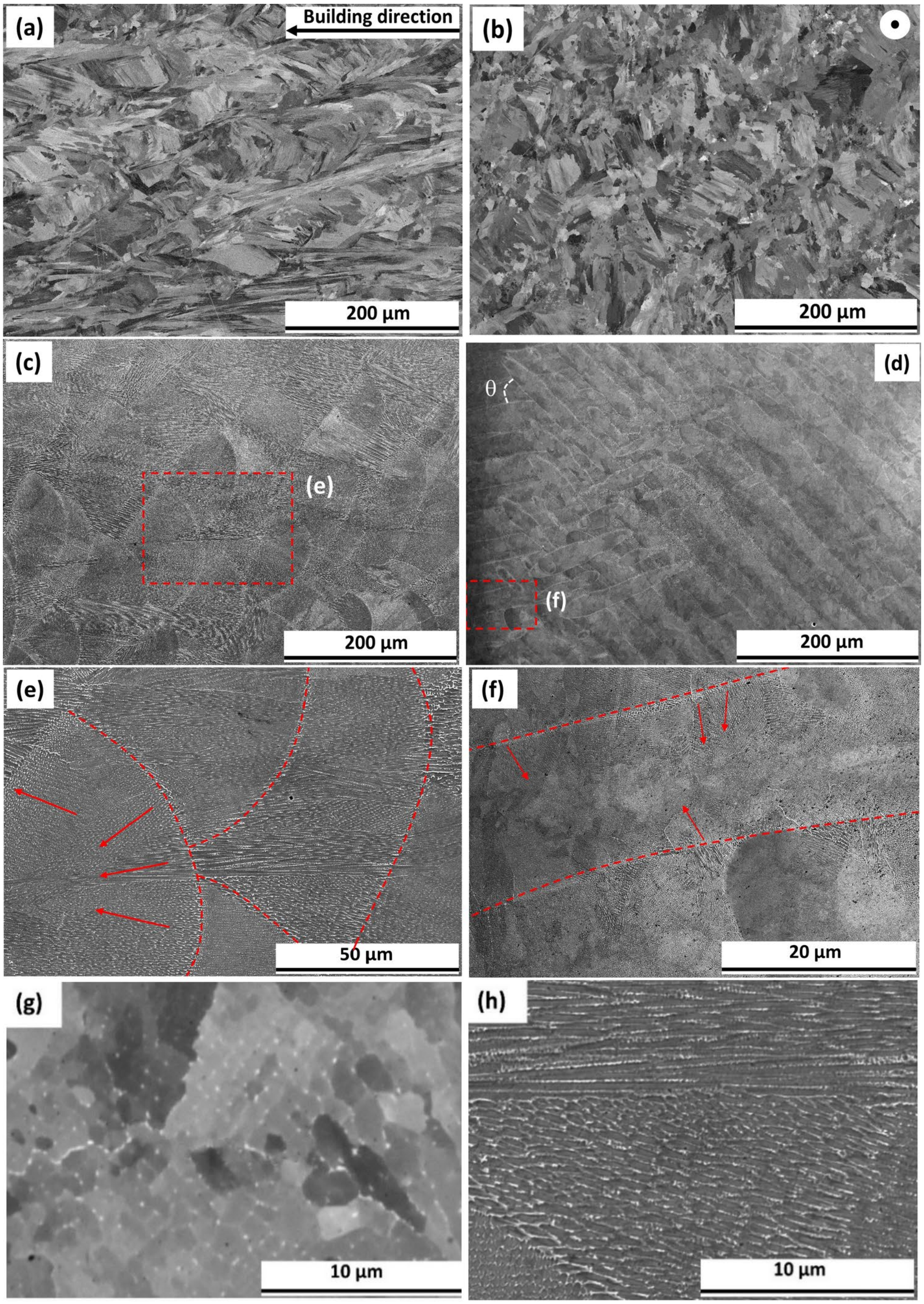

Fig. 7 Unetched microstructure of the as-built PBF-LB/IN718 manufactured in **a** horizontally and **b** vertically built orientation. Etched dendrite structure of as-built PBF-LB/IN718 in **c** horizontally and **d** vertically built orientation. The θ in (d) indicates the rotation angle between two neighboring layers. **e** and **f** The magnified areas marked in (c) and (d) respectively. Red arrows and dash lines in (e) and (f) presents the dendrite growth orientation and melt pool boundaries respectively. **g** and **h** The precipitation of Laves phase in the grain boundaries and the interdendritic regions of as-built PBF-LB/IN718 printed horizontally, respectively

exhibits a certain inclination relative to the build orientation; however, it does not necessarily align parallel to the building direction. On the other hand, the orientation of the grains in the vertically built sample seems to be irregular and random as illustrated in Fig. 7b.

After etching, the samples display a very fine dendritic structure, as shown in Fig. 7c and d. This structure is due to the fast heating and cooling rates involved in the PBF-LB process. The melt pool boundaries are visible in both vertically and horizontally built samples. The melt pools differ in size and growth direction of dendrites, as marked by red arrows in Fig. 7e and f. The dendrites develop in diverse directions, even inside a melt pool. The scanning direction was rotated by approximately 65° between two adjacent layers during manufacturing, as market by θ in Fig. 7d.

The magnified images (Fig. 7g and h) reveal that white particles have precipitated in both at the grains and the interdendritic regions. The XRD pattern of the as-built PBF-LB/IN718 reveals the presence of Laves as the secondary phases in the γ matrix as shown in Fig. 8. The microstructure and following white particles precipitates in this study are similar to those observed in other studies [15, 28]. These studies identify Laves and MC-type carbide as the white precipitates in the interdendritic regions of as-built PBF-LB/IN718. For example, Deng et al. [28] identified the precipitates in as-built PBF-LB/IN718 using TEM analysis. They found that the main precipitates in the as-built PBF-LB/IN718 are the Laves phases, with no indication of γ′ and γ″ precipitation as strengthening phases. Adomako et al. [15] identified some MC-type carbide precipitates along with Laves phases in the as-built PBF-LB/IN718 using EDS and TEM analysis. They found that Laves phases are long networked of white particle precipitates that are rich in Nb and other elements such as Fe and Cr whereas MC-type carbides such as (Nb, Ti) C are very fine, discrete, and globular particles rich in Ti and Nb. The XRD pattern of the AB sample confirms the presence of Laves phases along with the γ matrix as shown in Fig. 8. However, the diffraction pattern does not show any peaks for carbides due to possibly of their small quantity in the matrix.

3.2.2 Heat treated PBF-LB/IN718

As discussed in the previous section, as-built PBF-LB/IN718 is characterized by a large amount of Laves phases in the interdendritic zone due to the rapid solidification rate that hinders the precipitation of strengthening phases. Furthermore, residual stress also arises during the process due to the high thermal gradient and fast solidification rate. Therefore, heat treatment is needed to eliminate the residual stress and improve the mechanical properties of the alloy by promoting the precipitation of strengthening phases γ′ and γ″.

The microstructure of the heat treated PBF-LB/IN718 is shown in Fig. 9. It can be seen that the melt pool boundaries completely disappeared after the heat treatment and the dendritic features have been replaced by recrystallized grains. It should be noted that the volume of the

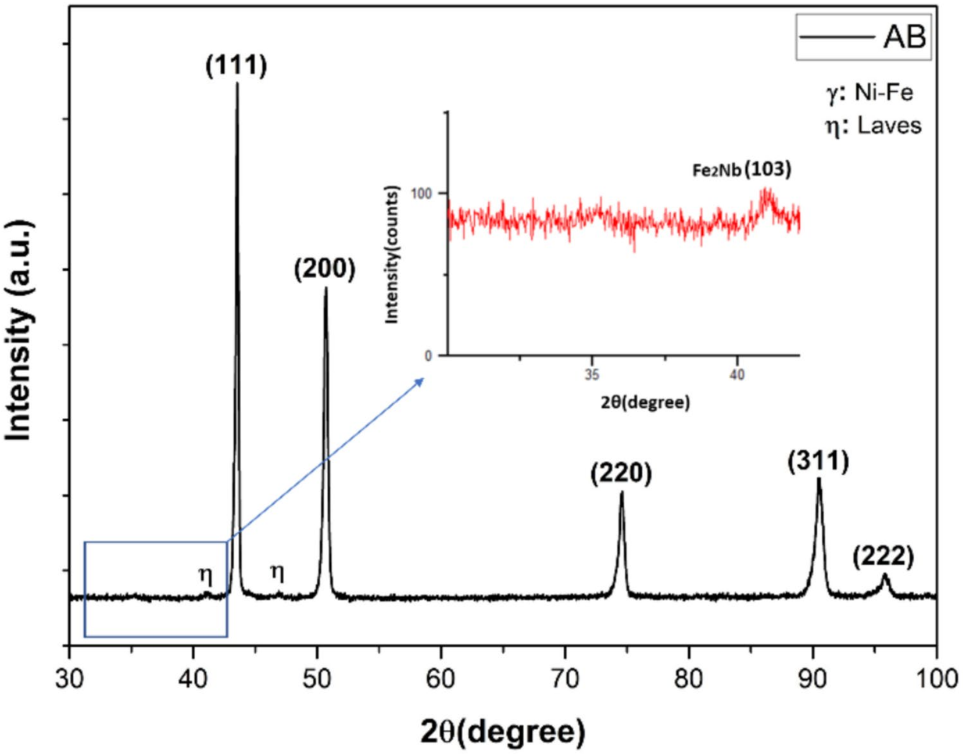

Fig. 8 The XRD pattern of the AB base metal

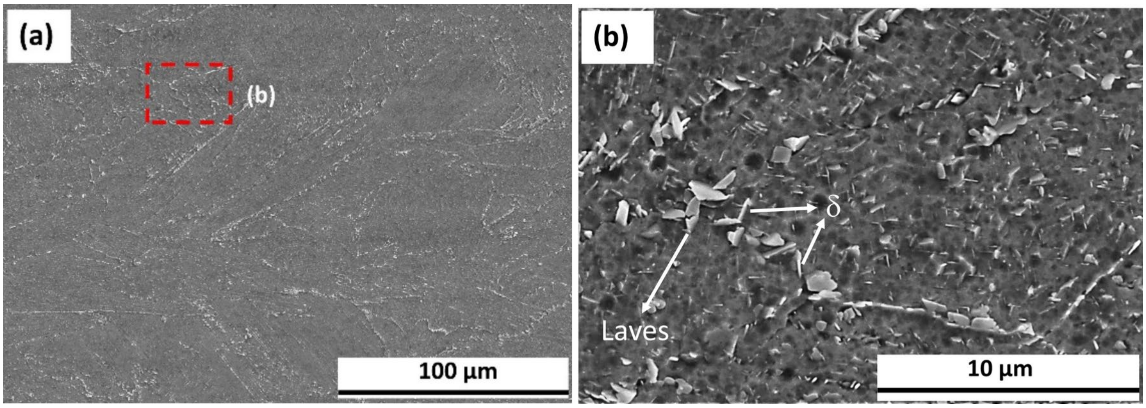

Fig. 9 **a** Microstructure of heat-treated PBF-LB/IN718 and **b** the magnified area indicated in (a) showing the presence of Laves and δ phases in interdendritic regions after heat-treatment

secondary phases is also reduced (Fig. 9a) compared to the as-built sample. This reduction indicates that heating the alloy up to 956 °C can dissolve the Laves phases. Dissolution of the Laves phase during the heat treatment results in more Nb being released into the matrix and thus more strengthening phases being precipitated in the alloy. However, some needle-shaped δ phases are also precipitated into the matrix after the heat treatments as shown in Fig. 9b. This precipitation means that the segregated Nb from the dissolved Laves phases is also consumed by δ phases, preventing further Nb inclusion into the γ″ phases. The precipitated δ phases are not coherent with the matrix, thereby affecting the mechanical properties of the alloy and serving as a suitable site for fracture development in tensile tests [29].

The presence of δ phases following the HT is confirmed by the XRD profile as shown in Fig. 10. It is noteworthy to mention that the absence of diffraction peaks for the Laves phase in the XRD pattern does not imply that they are entirely dissolved. The volume fraction of the Laves phase may have decreased to less than 5% following HT, which is subject to XRD detection limitations. The same principle applies for carbides which does not show diffraction peaks in the XRD profile. Deng et al. [28] solution treated the alloy at high temperature up to 980 °C and reported some traces of Laves phases remained in the alloy and concluded that solution temperature up to 1100 °C should be applied to the alloy in order to completely dissolve the Laves phases. Therefore, it is crucial to optimize the standard heat treatment mechanism, especially for additively manufactured IN718, to improve the mechanical properties of the alloy by controlling the precipitation of strengthening γ″ and γ′ phases and hindering the precipitation of detrimental Laves and δ phases.

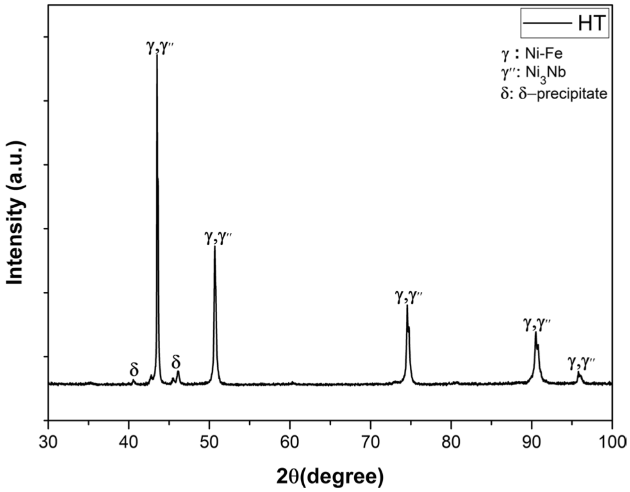

Fig. 10 The XRD pattern of the HT base metal

3.2.3 Welded joint of PBF-LB/IN718 and AISI 316L

The welded joints of PBF-LB/IN718 and AISI 316L are depicted in Fig. 11. The joint at low linear energy density of 75 J/mm (Fig. 11a) shows a columnar grain structure at the FZ whereas the joint at high linear energy density of 100 J/mm (Fig. 11b) shows equiaxed grain at the centerline of the FZ and columnar grain near the fusion line. The cooling rate is primarily responsible for this variation in grain morphology. At low linear energy density, the cooling rate is higher, resulting in faster solidification and less time for the formation of equiaxed grain morphology. It is important to note that both joints exhibit finer grain at the fusion line than the center line due to a larger thermal gradient and a higher temperature at the FZ center. During welding, the base materials will undergo a remelting and cooling cycle, dividing the weld zone into FZ and heat-affected zone (HAZ) as shown in

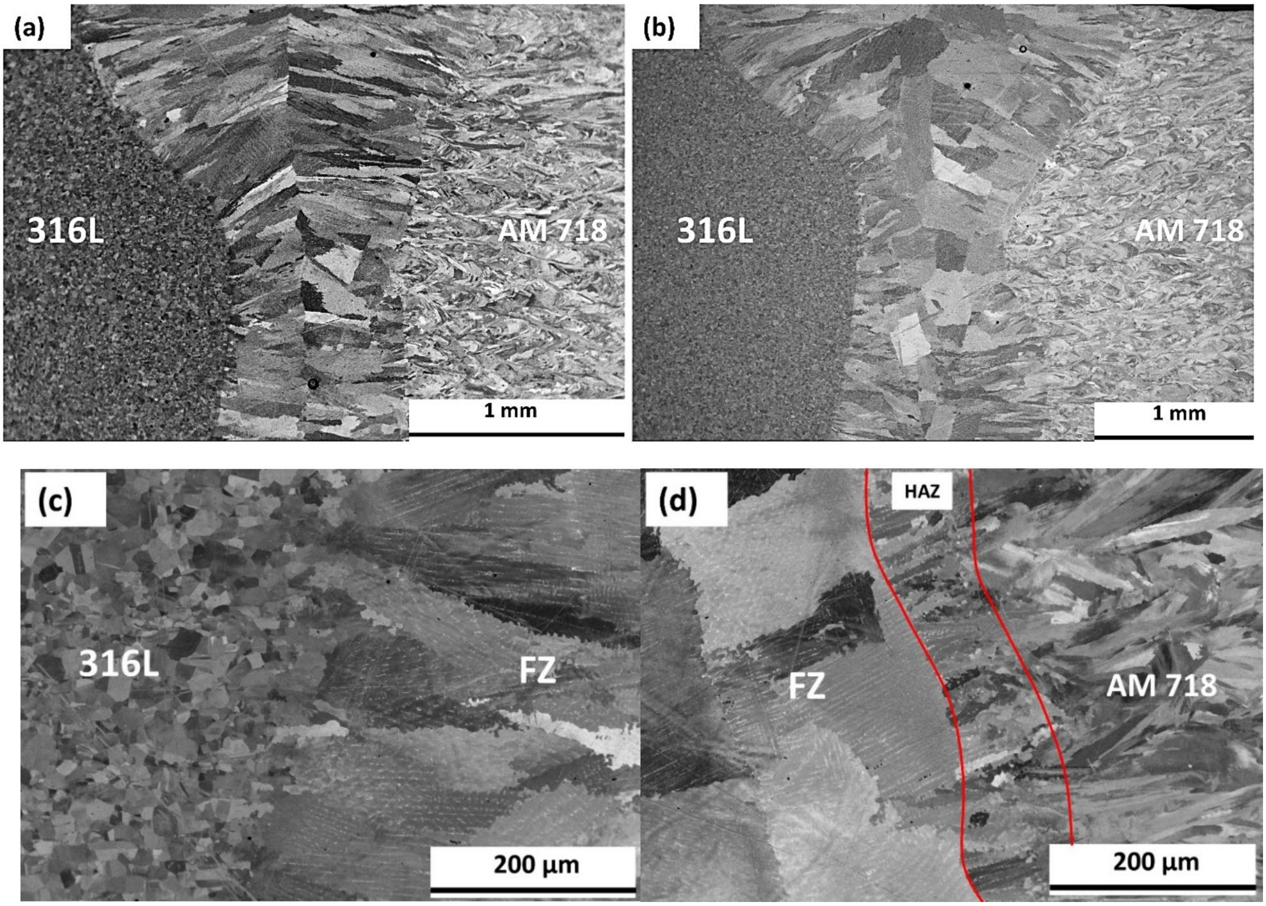

Fig. 11 Unetched microstructure of **a** the fusion zone, **b** the interface between FZ and base metal of PBF-LB/IN718, **c** the interface between FZ and base metal of AISI 316L

Fig. 11c and d. The HAZ in the PBF-LB/IN718 side shows elongated grains that are oriented towards the base metal. Furthermore, the size of the grains is smaller than that of the base metal; hence, recrystallization possibly occurred in such areas. In addition, some white particles are also precipitated in the HAZ of the PBF-LB/IN718 side, while there is no sign of such precipitations on the AISI 316L side.

The columnar-dendrite microstructure of the FZ is illustrated in Fig. 12. As shown in Fig. 12a, some secondary phases are found in the interdendritic region. The EDS elemental mapping shows that the interdendritic region consist of long networked particles that are rich in Nb (Fig. 12a) and some fine, discrete, and globular particle that are rich in Ti (Fig. 12c). The EDS point analysis shows the present of other alloying element such as Fe and Cr for the networked particles as listed in Table 6. Similar chemical composition at the FZ is reported by other researchers in which the long networked secondary phase, and discrete, spherical particles are identified as Laves and carbide respectively [15, 30]. It should be noted that the error associated with EDS measurements increases particularly when analyzing small precipitates such as MC as volume interaction of the EDS point is larger than the segregation itself; thus, the values reported in this study are not absolute and are reported as a semi-quantitate values. However, the EDS results are used to verify the phases' identification by XRD, and composition is compared with the available literature [28, 31]. The EDS point analysis (Table 6) shows that the amount of Nb in the Laves phases is almost five times higher than that of the base metal. The precipitation of the Laves phase and carbides at the FZ results in solidification cracking (microcracks) and weaken the joint strength as shown in Fig. 13. Solidification cracking arises primarily from the fact that precipitation of Laves and carbide (Nb, Ti) C increase the solidification range of the weld zone due to their lower solidus temperature (1198 °C) in comparison to the solidus temperature of alloy 718 (1369 °C) [31]. As a result, the presence of secondary phases lessens the ability of the joint to sustain the tensile stress during solidification, hence, promoting crack formation. Therefore, reducing the amount of Laves phases in the FZ will significantly enhance the microcrack sensitivity of the joints.

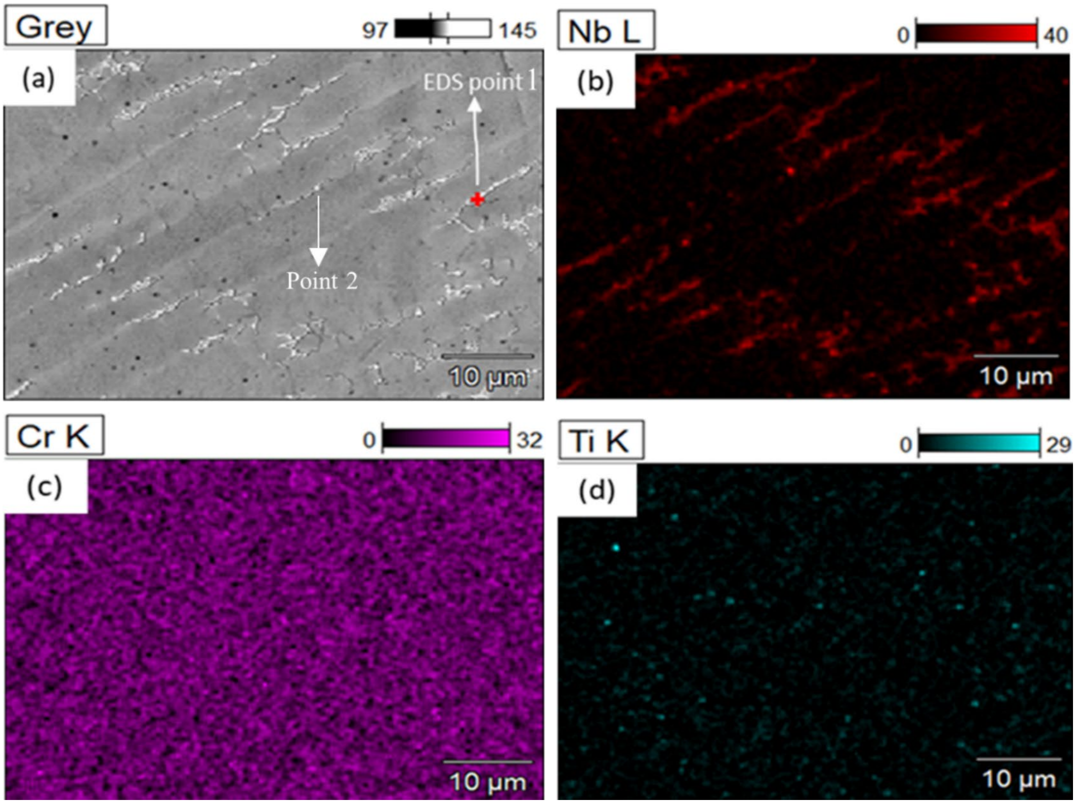

Fig. 12 EDS elemental mapping analysis of the fusion zone showing **a** the precipitation of the Laves phase (the red point is used for EDS point analyses for chemical composition of the Laves phases), **b** the distribution of Nb, **c** the distribution of Cr, **d** the distribution of Ti

Table 6 The chemical composition (wt%) of the Laves phase and carbides, detected in the point marked on Fig. 12a

Element	Ni	Fe	Cr	Nb	Mo	Ti	Al
Point 1	43.55	15.19	17.65	19.50	1.15	1.55	0.50
Point 2	37.68	11.45	10.89	23.56	3.80	12.65	0.10

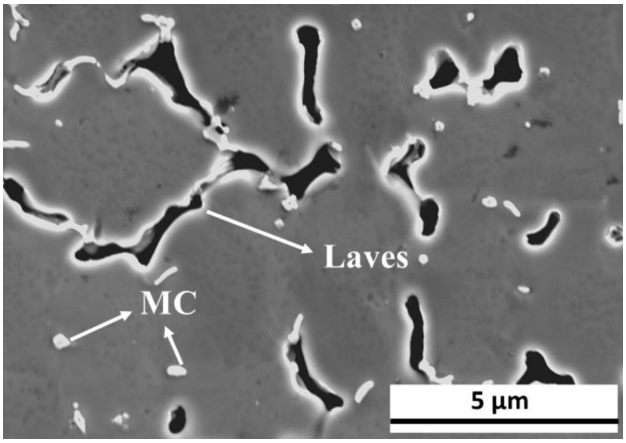

Fig. 13 SEM image of the micro cracks at the fusion zone

The XRD profile of the joints at the FZ is illustrated in Fig. 14. The diffraction peaks of the Laves and carbides are clearly identified in the XRD pattern which confirms the EDS elemental composition results. It should be noted that the diffraction peaks of γ′ and γ″ are overlapping with the γ matrix and its challenging to confirm the presence of strengthening phases at the FZ using XRD. The diffraction pattern at lower linear energy density (HTH1) shows a dominant texture in the [200] direction whereas the FZ at higher linear energy density (HTH3) shows a dominant texture in the [111] and [200] direction. This corresponds to the microstructure observation as the grain morphology at the FZ using lower linear energy density resulted in a very fine columnar microstructure (Fig. 11a) whereas the grain morphology at the FZ using higher linear energy density

Fig. 14 The XRD profile of HT joints at the FZ at linear energy density of 75 J/mm (HTH1) and 120 J/mm (HTH3)

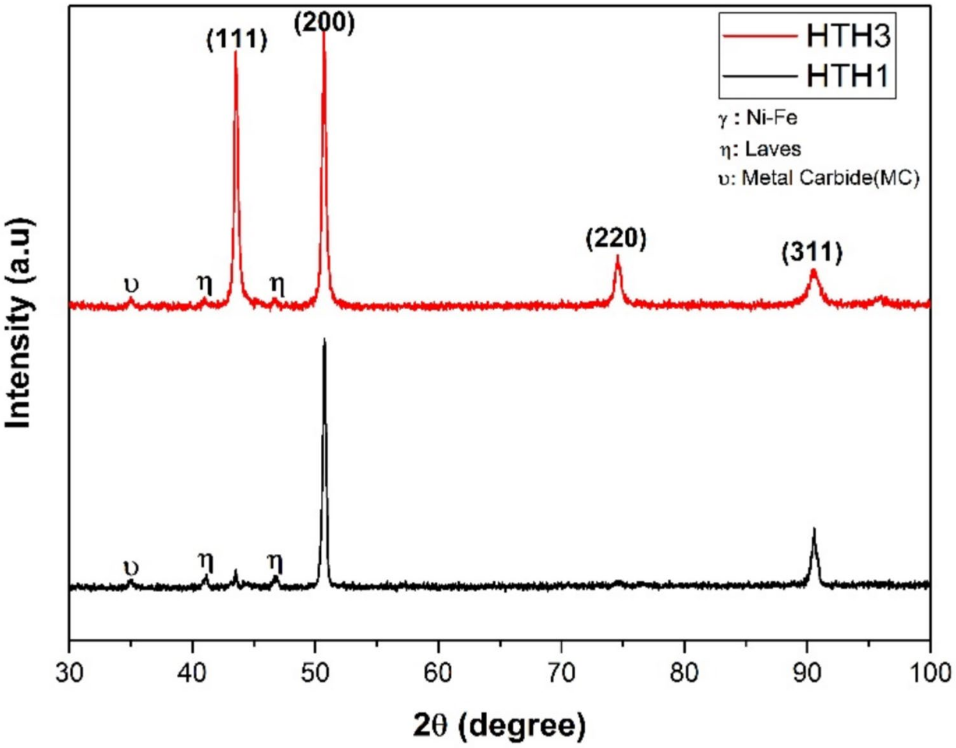

resulted in a mixture of columnar and equiaxed microstructure (Fig. 11b).

3.3 Mechanical properties

3.3.1 Microhardness measurements

The microhardness measurements of the joints for all energy densities are presented in Fig. 15. The microhardness value of the HT PBF-LB/IN718 as the base metal (450 HV) is higher than that of the as-built PBF-LB/IN718, as expected. The higher microhardness values in the HT samples are due to the dissolution of the Laves phases following the heat treatment, which releases more Nb into the γ matrix and causes the strengthening phase γ″ to precipitate. The average microhardness values at the 316L base metal are measured to be 150 HV. The average microhardness values at the FZ for all the joints are summarized in Table 7.

The results show that the average microhardness values of the AB and HT joints at the FZ are higher than the hardness value of the 316 L base metal indicating a high strength joint was achieved in all conditions. Furthermore, the HT joints appear to have lower hardness values than the AB joints in all three different linear energy density conditions. This might be due to the different secondary phases in the samples prior welding. The heat cycle during welding may dissolve the Laves phases in the AB base metal thus more Nb would be available for the strengthening phases to precipitate. On the other hand, the welding heat cycle may dissolve the strengthening phases that are already precipitated in the HT base metal following heat treatment and results in lower microhardness after welding. In a similar study by Cao et al. [31], it is reported that the higher amount of Laves phases at the FZ of the heat-treated joints could result in less Nb segregation into the matrix which in turn leads to less strengthening phases' precipitation. Therefore, the HT prior welding is not recommended for this particular joint in this study.

In addition, the microhardness values of the joints at higher linear energy density conditions exhibit slight variations depending on their built orientation. In the case of AB joints, it is observed that vertically made samples possess marginally higher microhardness values than the horizontally made ones. The ABV joints showed the highest microhardness values for all three energy densities among all the joints. In the case of HT joints, there are no specific patterns since the vertically made joints (HTV) exhibit superior microhardness at a linear energy density of 100 J/mm, whereas the horizontally made joints (HTH) show superior microhardness at a linear energy density of 120 J/mm.

3.3.2 Tensile performance

Figure 16 exhibits the engineering stress–strain curve of the joints in relation to the linear energy density. All the joints at lower linear energy density of 75 J/mm failed at the AISI

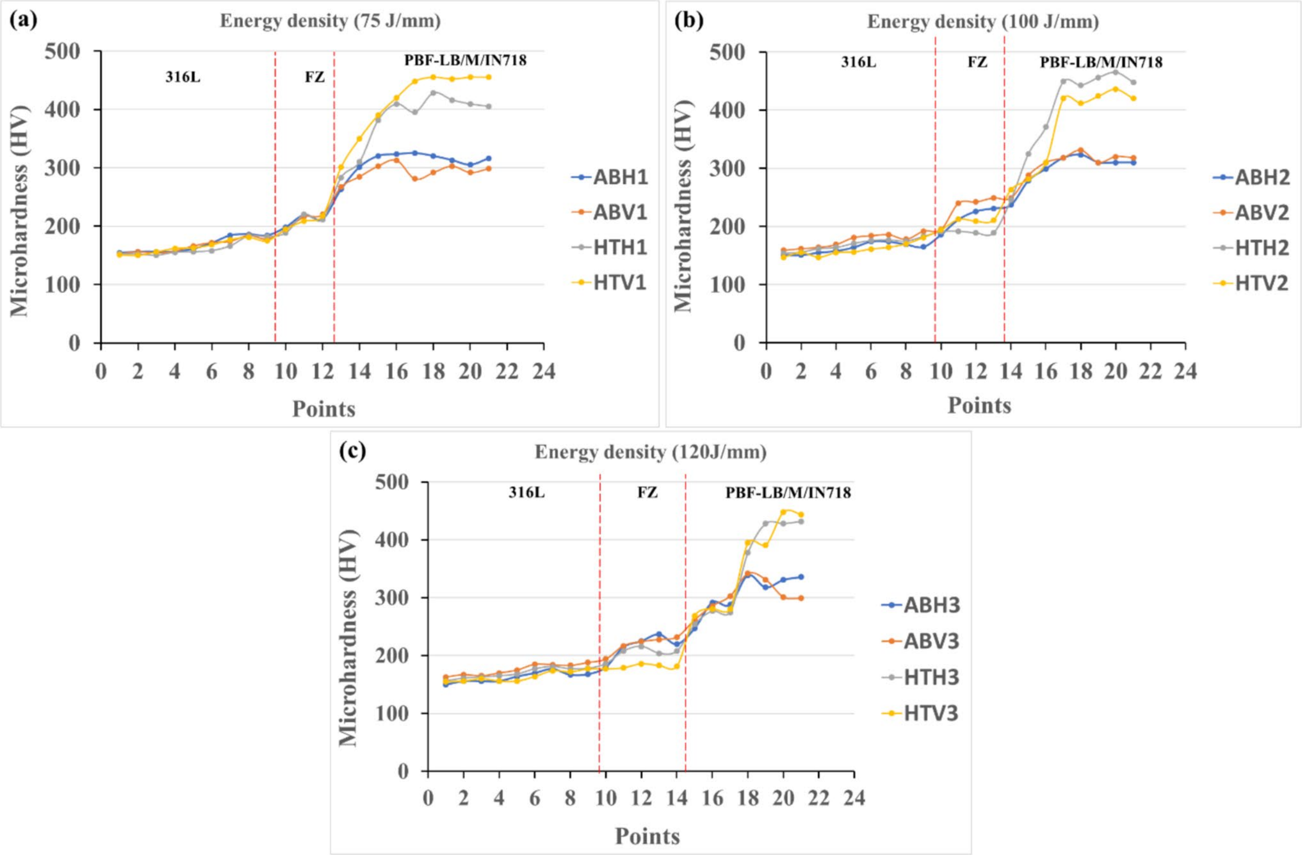

Fig. 15 The hardness value in the base metals and fusion zone for the samples that are welded at linear energy density of **a** 75 J/mm, **b** 100 J/mm, **c** 120 J/mm

Table 7 Average hardness values at the fusion zone for all the joints (unit is in HV)

Laser parameters	ABH	ABV	HTH	HTV
#1	210 ± 7	210 ± 8	206 ± 12	205 ± 5
#2	218 ± 12	230 ± 10	190 ± 4	200 ± 7
#3	215 ± 10	219 ± 12	201 ± 10	185 ± 8

316L base metal, indicating a strong joint at the weld zone (Fig. 16a). However, by increasing the linear energy density, two different trends are observed: the HT joints failed at the FZ, whereas the AB joints failed at the AISI 316L base metal. In other words, the AB joints failed at the AISI 316L base metal for all three different linear energy density parameters, demonstrating a strong joint, while the HT joints failed at the FZ at higher energy densities of 100 and 120 J/mm, indicating that high linear energy density weakens the weld strength of the HT joints.

The tensile properties of all joints as a function of the linear energy density parameters are presented in Fig. 17. These results illustrate that ultimate tensile strength (UTS) of the AB joins are higher than the HT joints particularly at higher linear energy density parameters (Fig. 17b) signifying a better weld strength at the low linear energy density of 75 J/mm in both AB and HT joints. This is in consistent with the hardness results as the AB joints showed higher hardness than the HT joints. Moreover, the ductility of the HT joints at higher energy densities is significantly declined as shown in Fig. 17c. The fracture surface examination of the HT joints revealed the presence of large porosities of size of 200–300 µm as well as many small pores as seen in Fig. 18. The HT joints appear to be more prone to pore formation than the AB joints. Porosity formation particularly during welding for Ni-based alloys has been reported by other studies [14, 15]. It is mainly caused by the poor fluidity of the Ni-based alloys due to their high viscosity. As a result, pores formed during laser welding do not have enough time to escape from the keyhole and get trapped into the molten pool. According to some studies, there are two main mechanisms for the pore formation, namely keyhole induced porosity and metallurgical pores [32–34]. Li et al. [35] reported that both metallurgical and

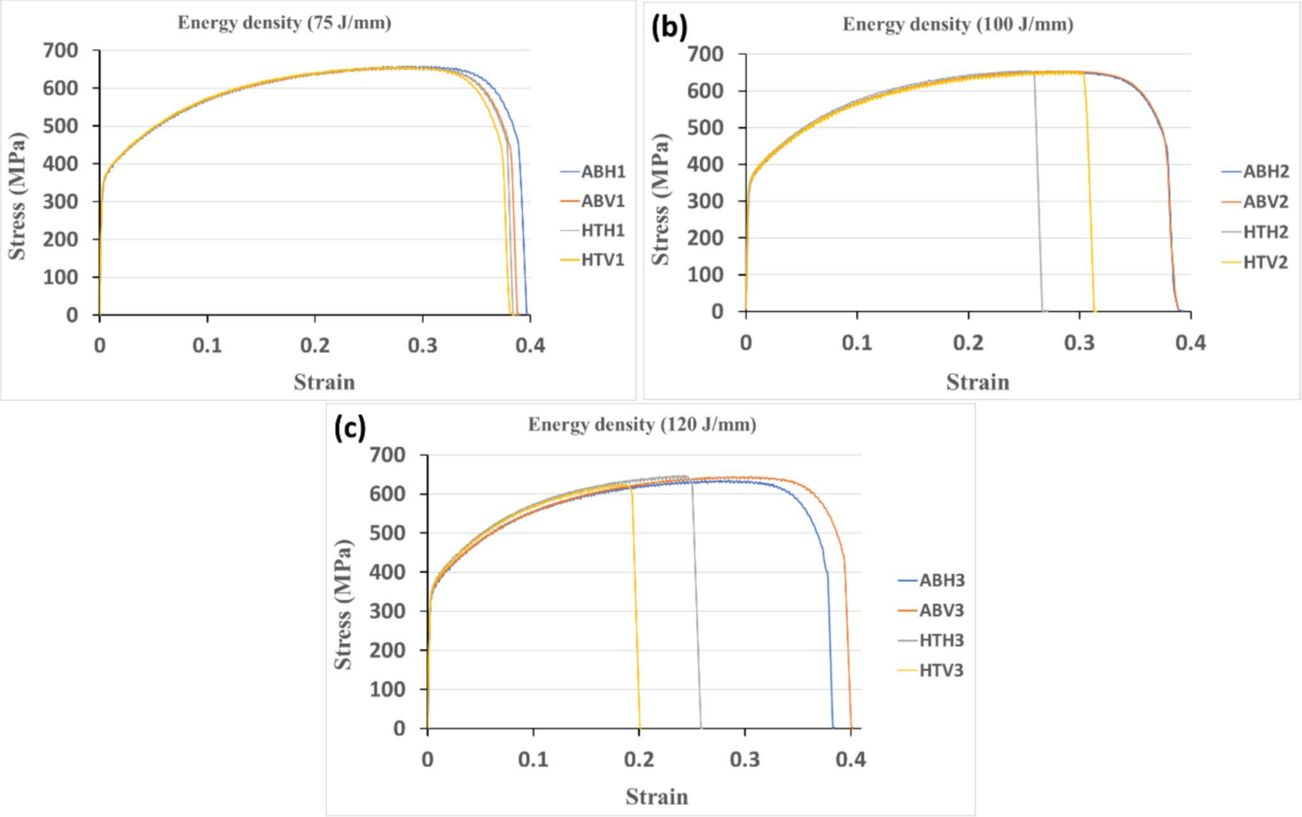

Fig. 16 Stress–strain curve of the joints which are welded at linear energy density of **a** 75 J/mm, **b** 100 J/mm, **c** 120 J/mm

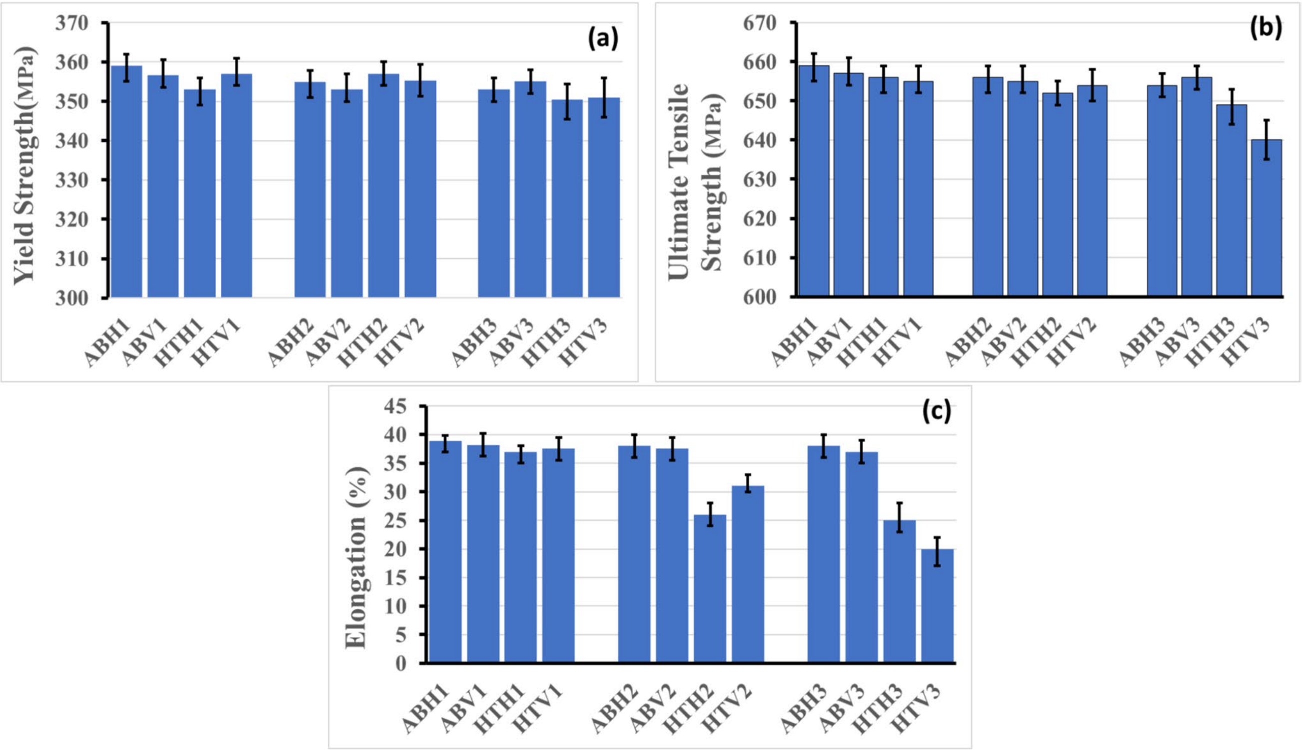

Fig. 17 The ultimate, yield strength and elongation of joints at linear energy density of **a** 75 J/mm, **b** 100 J/mm, **c** 120 J/mm

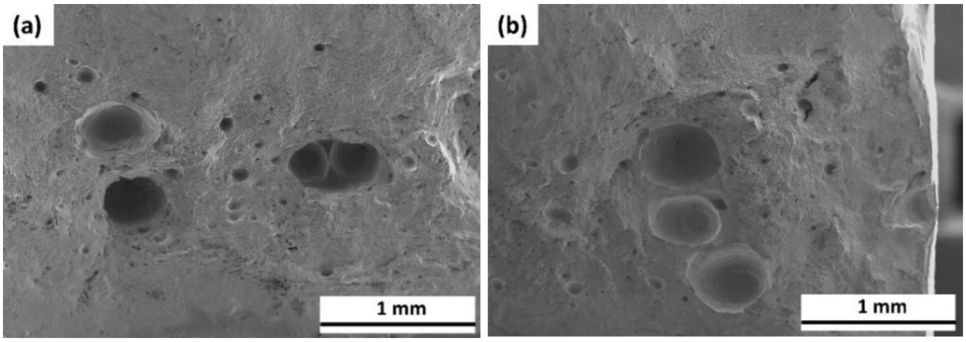

Fig. 18 SEM images of the fracture surface of HT joints **a** HTH3, **b** HTV2

keyhole induced porosities were observed during hybrid MIG-laser welding of IN718. It was concluded that the metallurgical pores were related to the active elements on the surface of the samples and environment such as O and H_2O in which the interaction of C and O in the molten pool resulted in gas bubble pores, and the keyhole-induced pores were mostly correlated to the laser parameters particularly laser powers, and it was inferred that higher welding power leads to higher degree of instability of the keyhole; therefore, more pores forms in the joint. A similar observation was also reported by Cao et al. [31] in which the HT joints exhibited more porosity than the as-received joints. This is in line with the finding in Sect. 3.1, wherein more spatter was observed in the HT joints due to the surface contamination following the heat treatment process. Therefore, it could be concluded that the incomplete oxide layer removal process which was employed in this work is the main cause for higher porosity in the HT joints which in turn impacted the mechanical properties of the HT joints. Therefore, oxide layer removal should be carefully taken care of prior to welding to prevent such joint failures. It is worth mentioning that in absence of porosities, the microcracks results from Laves phases and carbides are the most important factors that could weaken the joint strength as reported in other researches [14, 15]. However, since the porosities were the primary cause of failure in the HT joints, it was not possible to investigate the impact of microcracks following the secondary phases' precipitations on mechanical properties.

No major difference is observed between the joints in relation to the build orientation of the PBF-LB/IN718 samples, implying that mechanical properties of the joints are not affected by the build orientation. However, the HTV3 joints shows the lowest ultimate strength values compared to all other joints due to the incomplete filled groove that was observed in this particular joint (Fig. 5f). Hence, it can be implied that the vertically made samples could be more sensitive to high input energies than the horizontally made ones. However, this assumption needs to be further studied and clarified by implementing higher energy inputs than those used in this research.

4 Conclusion

In this study, laser welding has been utilized to join PBF-LB/IN718 to AISI 316L. The microstructure and mechanical characteristic of the joints have been examined to understand the effect of build orientation, laser linear energy density, and heat treatment on the weld joint strength. The primary results of the study can be outlined as follows:

- Linear energy density plays a crucial role in achieving a sound joint. The dissimilar joints in this study using a low linear energy density of 75 J/mm resulted in the highest joint strengths; hence, low linear energy density condition is recommended for this particular dissimilar welding.
- The AB joints showed a superior mechanical performance compared to the HT joints, particularly at high heat inputs of 100 and 120 J/mm, due to higher microhardness and less pores at the FZ. The residual oxide contamination on the HT surface following the heat treatment process inferred to be the main reason for the inferior joint strength in the HT joints, which led to formation of higher degree of porosities in the FZ of the HT joints.
- The ductility and UTS of the AB joints were comparable at all linear energy density conditions, indicating a sound joint could be achieved in the AB condition using different laser parameters, whereas the HT joints showed higher sensitivity to laser parameters as the ductility were significantly dropped at high linear energy density of 100 and 120 J/mm.
- There is no significant change in the mechanical characteristics of the joints in relation to the PBF-LB/IN718 build orientation, implying that sample orientation has no major impact on the joint strength.

Acknowledgements The authors would like to thank Mr. Olli-Pekka Pynnönen for performing the tensile tests and Dr. Ilkka Poutiainen for conducting the laser welding of the specimens. This work was carried out by the LUT University, the University of Turku, and industrial partners.

Author contribution Saeid Parchegani: writing—review and editing, writing—original draft, investigation, formal analysis, data curation, conceptualization. Mohsen Amraei: formal analysis. Shahriar Afkhami: formal analysis, conceptualization. Heidi Piili: supervision, writing—review and editing. Antti Salminen: funding acquisition, supervision.

Funding Open Access funding provided by University of Turku (including Turku University Central Hospital). This research was done as part of the CaNeLis project (carbon–neutral lightweight ship structures using advanced design, production, and life-cycle services) funded by business Finland, and the Verkota project (Verkostoitumisella voimaa) funded by the European Regional Development Fund (ERDF).

Data availability The data that support the findings of this study are available upon reasonable request.

Declarations

Competing interests The authors declare no competing interests.

References

1. Benedetti M, Fontanari V, Bandini M, Zanini F, Carmignato S (2018) Low-and high-cycle fatigue resistance of Ti-6Al-4V ELI additively manufactured via selective laser melting: mean stress and defect sensitivity. Int J Fatigue 107:96–109
2. Yang J, Yang H, Yu H, Wang Z, Zeng X (2017) Corrosion Behavior of Additive Manufactured Ti-6Al-4V Alloy in NaCl Solution. Metall Mater Trans A 48:3538–3593
3. Parchegani S, Piili H, Ganvir A, Salminen A, Conf IOP (2023) Laser welding of additively manufactured parts-A review. Mater Sci Eng 1296:012030. https://doi.org/10.1088/1757-899X/1296/1/012030
4. Wei HL, Elmer JW, DebRoy T (2017) Crystal growth during keyhole mode laser welding. Acta Mater 133:10–20
5. Shao L, Datye A, Huang J, Ketkaew J, Sohn SW, Zhao S, Wu S, Zhang Y, Schwarz UD, Schroers J (2017) Pulsed laser beam welding of Pd43Cu27Ni10P20 bulk metallic glass. Sci Rep 7:7989
6. Ramkumar KD, Patel SD, Praveen SS, Choudhury DJ, Prabaharan P, Arivazhagan N, Xavior MA (2014) Influence of filler metals and welding techniques on the structure-property relationships of Inconel 718 and AISI 316L dissimilar weldments. Mater Design 62:175–188
7. Ramkumar T, Selvakumar M, Narayanasamy P, Begam AA, Mathavan P (2017) Studies on the structural property, mechanical relationships and corrosion behavior of Inconel 718 and SS 316L dissimilar joints by TIG welding without using activated flux. J Manuf Process 30:290–298
8. Henderson MB, Arrellb D, Larsson R, Heobel M, Marchant G (2004) Nickel-based superalloy welding practices for industrial gas turbine applications. Sci Technol Weld Joi 9(1):13–21
9. Locci IE, Bowman CL, Gabbs TP (2009) Development of high temperature dissimilar joint technology for fission surface power systems Proceedings of the 4th International Brazing and Soldering Conference, April 26–29, Hilton in the Walt Disney World Resort, Orlando, Florida. USA
10. Ferretti S, Valenzano G, Cugno W (2006) International space station external active thermal control system lines manufacturing, the 57th International Astronautical Congress Proceeding, October 2–6 Valencia, Spain
11. Leary RK, Merson E, Birmingham K, Harvey D, Brydson R (2010) Microstructural and microtextural analysis of InterPulse GTCAW welds in Cp-Ti and Ti–6Al–4V. Mater Sci Eng A 527:7694–7705. https://doi.org/10.1016/j.msea.2010.08.036
12. Radhakrishna CH, Prasad Rao K (1997) The formation and control of Laves phase in superalloy 718 welds. J Mater Sci 32:1977–1984. https://doi.org/10.1023/A:1018541915113
13. Devendranathramkumar K, Sridhar R, Periwal S, Oza S, Saxena V, Hidad P, Arivazhagan N (2015) Investigations on the structure – property relationships of electron beam welded Inconel 625 and UNS 32205. Mater Design 68:158–166. https://doi.org/10.1016/j.matdes.2014.12.032
14. Kuo TY (2005) Effects of pulsed and continuous Nd–YAG laser beam waves on welding of Inconel alloy. Sci Technol Weld Join 10. https://doi.org/10.1179/174329305X46709
15. Adomako NK, Park HJ, Cha SC, Lee M, Kim JH (2021) Microstructure evolution and mechanical properties of the dissimilar joint between IN718 and STS304. Mater Sci Eng A 799:140262. https://doi.org/10.1016/j.msea.2020.140262
16. Matilainen V, Pekkarinen J, Salminen A (2016) Weldability of additive manufactured stainless steel. Phys Procedia 83:808–817. https://doi.org/10.1016/j.phpro.2016.08.083
17. Yang J, Wang Y, Li F, Huang W, Jing G, Wang Z, Zeng X (2019) Weldability, microstructure and mechanical properties of laser-welded selective laser melted 304 stainless steel joints. J Mater Sci Technol 35(9):1817–1824. https://doi.org/10.1016/j.jmst.2019.04.017
18. Wits WW, Jauregui Becker JM (2015) Laser beam welding of titanium additive manufactured parts. Procedia CIRP 28:70–75. https://doi.org/10.1016/j.procir.2015.04.013
19. Yu H, Li F, Yang J, Shao J, Wang Z, Zeng X (2018) Investigation on laser welding of selective laser melted Ti-6Al-4V parts: weldability, microstructure and mechanical properties. Mater Sci Eng A 712:20–27. https://doi.org/10.1016/j.msea.2017.11.086
20. Biffi CA, Fiocchi J, Tuissi A (2019) Laser weldability of $AlSi_{10}Mg$ alloy produced by selective laser melting: microstructure and mechanical behavior. J Mater Eng Perform 28:6714–6719. https://doi.org/10.1007/s11665-019-04402-7
21. Voropaev A, Stramko M, Sorokin A, Logachev I, Kuznetsov M, Gook S (2020) Laser welding of Inconel 718 nickel-based alloy layer-by-layer products. Mater Today Proc 30:473–477. https://doi.org/10.1016/j.matpr.2019.12.399
22. Jokisch T, Marko A, Gook S, Üstündag Ö, Gumenyuk A, Rethmeier M (2019) Laser welding of SLM-manufactured tubes made of IN625 and IN718. Materials 12:2967. https://doi.org/10.3390/ma12182967
23. Jiang R, Mostafaei A, Wu Z, Choi A, Guan PW, Chmielus M, Rollett AD (2020) Effect of heat treatment on microstructural evolution and hardness homogeneity in laser powder bed fusion of alloy718. Addit Manufact 35:101282. https://doi.org/10.1016/j.addma.2020.101282
24. Parviainen J (2021) The effects of laser welding parameters on the weldability of AM IN718 TO WROUGHT 316L steel, Master

thesis, LUT university. https://lutpub.lut.fi/handle/10024/162968?show=full.

25. Zhang Y, Chen J, Zhang W, Li C, Qiu C, Ding J, Lu H, Zhang K (2023) Study of spatter net forming mechanism and penetration mode under flexible ring mode laser welding. J Mater Res Technol 24:2213–2225. https://doi.org/10.1016/j.jmrt.2023.03.139
26. Kaplan A, Powell J (2011) Spatter formation in laser welding. J Laser Appl https://doi.org/10.2351/1.3597830.
27. Kathiravan S, Kaliaraj Gobi Saravanan, Kamalan Kirubaharan AM, Kumar Ravi Ranjan (2022) Study of oxide layer formation on Inconel 718 during isothermal oxidation between 800 °C to 1200 °C in hot air. Ceram Int 48(24):36012–36020. https://doi.org/10.1016/j.ceramint.2022.07.187
28. Deng D, Peng RL, Brodin H, Moverare J (2018) Microstructure and mechanical properties of Inconel 718 produced by selective laser melting: sample orientation dependence and effects of post heat treatments. Mater Sci Eng A 713:294–306. https://doi.org/10.1016/j.msea.2017.12.043
29. Garcia C, Lis A, Loria E, DeArdo A (1992) Thermomechanical processing and continuous cooling transformation behavior of in 718, in: Proceedings of the Conference Superalloys, 527–536
30. Zhao D, Liu F, Tan Y, Shi W, Xiang S (2023) Improving the strength-ductility synergy and corrosion resistance of Inconel 718/316L dissimilar laser beam welding joint via post-weld heat treatment. J Mater Res Technol 26:71–87. https://doi.org/10.1016/j.jmrt.2023.07.202
31. Cao X, Rivaux B, Jahazi M, Cuddy J, Birur A (2009) Effect of pre- and post-weld heat treatment on metallurgical and tensile properties of Inconel 718 alloy butt joints welded using 4 kW Nd:YAG laser. J Mater Sci 44:4557–4571
32. Jiang M, Chen X, Chen Y et al (2020) Mitigation of porosity defects in fiber laser welding under low vacuum. J Mater Process Technol 276:116385
33. Zhang C, Yu Y, Chen C et al (2020) Suppressing porosity of a laser keyhole welded Al-6Mg alloy via beam oscillation. J Mater Process Technol 278:116382
34. Kaplan A, Mizutani M, Katayama S, Matsunawa A (2002) Unbounded keyhole collapse and bubble formation during pulsed laser interaction with liquid zinc. J Phys D Appl Phys 35:1218. https://doi.org/10.1088/0022-3727/35/11/319
35. Li Y, Li Y, Feng Y et al (2024) Investigation on the morphology and formation mechanism of porosity in different heat source regions of nickel-based alloy laser hybrid welding. J Materi Eng and Perform 33:6432–6441. https://doi.org/10.1007/s11665-023-08409-z